

Membrane assembly of aquaporin-4 autoantibodies regulates classical complement activation in neuromyelitis optica

John Soltys, ... , Gregory P. Owens, Jeffrey L. Bennett

J Clin Invest. 2019;129(5):2000-2013. <https://doi.org/10.1172/JCI122942>.

Research Article

Inflammation

Neuroscience

Neuromyelitis optica (NMO) is an autoimmune CNS disorder mediated by pathogenic aquaporin-4 (AQP4) water channel autoantibodies (AQP4-IgG). Although AQP4-IgG-driven complement-dependent cytotoxicity (CDC) is critical for the formation of NMO lesions, the molecular mechanisms governing optimal classical pathway activation are unknown. We investigated the molecular determinants driving CDC in NMO using recombinant AQP4-specific autoantibodies (AQP4 rAbs) derived from affected patients. We identified a group of AQP4 rAbs targeting a distinct extracellular loop C epitope that demonstrated enhanced CDC on target cells. Targeted mutations of AQP4 rAb Fc domains that enhance or diminish C1q binding or antibody Fc-Fc interactions showed that optimal CDC was driven by the assembly of multimeric rAb platforms that increase multivalent C1q binding and facilitate C1q activation. A peptide that blocks antibody Fc-Fc interaction inhibited CDC induced by AQP4 rAbs and polyclonal NMO patient sera. Super-resolution microscopy revealed that AQP4 rAbs with enhanced CDC preferentially formed organized clusters on supramolecular AQP4 orthogonal arrays, linking epitope-dependent multimeric assembly with enhanced C1q binding and activation. The resulting model of AQP4-IgG CDC provides a framework for understanding classical complement activation in human autoantibody-mediated disorders and identifies a potential new therapeutic avenue for treating NMO.

Find the latest version:

<https://jci.me/122942/pdf>



Membrane assembly of aquaporin-4 autoantibodies regulates classical complement activation in neuromyelitis optica

John Soltys,¹ Yiting Liu,² Alanna Ritchie,² Scott Wemlinger,² Kristin Schaller,² Hannah Schumann,² Gregory P. Owens,² and Jeffrey L. Bennett^{1,2,3}

¹Neuroscience and Medical Scientist Training Programs, ²Department of Neurology, and ³Department of Ophthalmology, University of Colorado at Anschutz Medical Campus, Aurora, Colorado, USA.

Neuromyelitis optica (NMO) is an autoimmune CNS disorder mediated by pathogenic aquaporin-4 (AQP4) water channel autoantibodies (AQP4-IgG). Although AQP4-IgG-driven complement-dependent cytotoxicity (CDC) is critical for the formation of NMO lesions, the molecular mechanisms governing optimal classical pathway activation are unknown. We investigated the molecular determinants driving CDC in NMO using recombinant AQP4-specific autoantibodies (AQP4 rAbs) derived from affected patients. We identified a group of AQP4 rAbs targeting a distinct extracellular loop C epitope that demonstrated enhanced CDC on target cells. Targeted mutations of AQP4 rAb Fc domains that enhance or diminish C1q binding or antibody Fc-Fc interactions showed that optimal CDC was driven by the assembly of multimeric rAb platforms that increase multivalent C1q binding and facilitate C1q activation. A peptide that blocks antibody Fc-Fc interaction inhibited CDC induced by AQP4 rAbs and polyclonal NMO patient sera. Super-resolution microscopy revealed that AQP4 rAbs with enhanced CDC preferentially formed organized clusters on supramolecular AQP4 orthogonal arrays, linking epitope-dependent multimeric assembly with enhanced C1q binding and activation. The resulting model of AQP4-IgG CDC provides a framework for understanding classical complement activation in human autoantibody-mediated disorders and identifies a potential new therapeutic avenue for treating NMO.

Introduction

Neuromyelitis optica (NMO) is an inflammatory disorder of the CNS that commonly presents with recurrent attacks of optic neuritis or transverse myelitis (1). Approximately 80% of patients are seropositive for autoantibodies (AQP4-IgG) targeting aquaporin-4 (AQP4), the predominant homeostatic water channel of the CNS (2–4). CNS histopathology and experimental data support a direct role for AQP4-IgG in NMO pathogenesis (3, 5, 6).

While AQP4-IgG may cause astrocyte injury through multiple mechanisms (6, 7), both clinical and experimental data indicate that AQP4-IgG-mediated classical complement activation is the primary mechanism initiating CNS injury. Classical pathway activation begins when the multivalent protein C1q binds to conformational Fc determinants on IgG or IgM antibody-antigen complexes. This triggers a proteolytic cascade that ultimately produces an array of biologically active proteins: opsonins, anaphylatoxins, chemotaxins, and the membrane attack complex (8, 9). In vivo and ex vivo models of NMO lesion formation are dependent on the initiation of complement-dependent cytotoxicity (CDC) (10–14).

AQP4-IgG-mediated CDC is dependent on the assembly of cell-surface AQP4 tetramers into supramolecular orthogonal array of particles (OAPs). AQP4 tetramers are composed of 2 isoforms: a full-length M1 and a shorter M23 protein (15). M1- and M23-AQP4 possess identical extracellular domains and differ only by a 22-amino acid, intracellular N-terminal sequence. M23-AQP4 promotes and M1-AQP4 limits the organization of AQP4 into OAPs. Classical complement activation by AQP4-IgG occurs only on plasma membrane OAPs, presumably because the larger arrays permit denser AQP4-IgG binding to enhance multivalent interactions with C1q (12, 16, 17). However, serum AQP4-IgG titers do not correlate directly with CDC, suggesting that AQP4 autoantibodies may not bind or activate C1q equally (18). Indeed, there exists significant microheterogeneity among the conformational epitopes recognized by individual AQP4 autoantibodies (19, 20), resulting in distinct affinities for AQP4 OAPs and tetramers (21, 22). Therefore, while most AQP4 autoantibodies are IgG1, AQP4 epitope specificity may modulate CDC by facilitating C1q binding or activation (16).

Although a definitive model of C1q activation by IgG is lacking (23, 24), recent studies have indicated that the ordered assembly of IgG hexamers on membrane targets yields a best-fit model for C1q binding and activation (25). While the model has guided the generation of novel, highly efficient antibody therapeutics (26–28), it remains uncertain whether natural circulating antibodies exploit similar mechanisms to engage and activate C1q. We made use of human monoclonal AQP4 recombinant autoantibodies (rAbs) generated from cerebrospinal fluid plasmablasts obtained

Conflict of interest: JLB serves as a consultant for Clene Nanomedicine, MedImmune, Chugai Pharmaceutical, EMD Serono, Equillum, and Frequency Therapeutics; receives research support from Mallinckrodt; and serves on the editorial boards of the *Multiple Sclerosis Journal*, *Neurology: Neuroimmunology & Neuroinflammation*, and the *Journal of Neuro-Ophthalmology*.

Copyright: © 2019, The American Society for Clinical Investigation.

Submitted: June 15, 2018; **Accepted:** February 26, 2019; **Published:** April 8, 2019.

Reference information: *J Clin Invest.* 2019;129(5):2000–2013.

<https://doi.org/10.1172/JCI122942>.

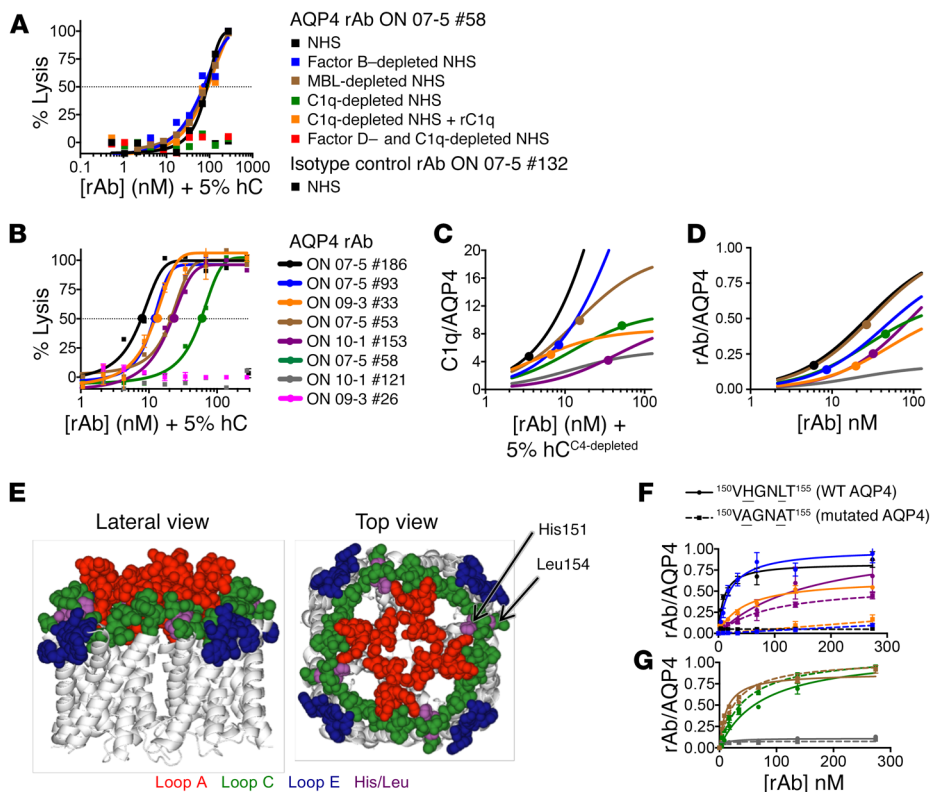


Figure 1. AQP4 rAb binding and classical complement activation on M23-AQP4 CHO cells. (A) CDC of M23-AQP4 CHO cells induced by AQP4 rAb ON 07-5 no. 58 or isotype control rAb ON 07-5 no. 132 was quantified using an lactate dehydrogenase (LDH) release assay (mean \pm SEM; $n = 4$). Complete or depleted preparations of NHS were used as sources of complement proteins. Recombinant complement C1q (rC1q) was added where indicated. The dashed line indicates 50% lysis. (B) CDC induced by monoclonal AQP4 rAbs with differing epitope specificities measured using an LDH release assay (mean \pm SEM; $n = 4$). The dashed line indicates 50% lysis. (C) The ratio of bound C1q to AQP4 is plotted against the rAb concentration. Solid circles indicate the CDC EC_{50} for complement activation. (D) The ratio of bound rAb to cell-surface AQP4 (rAb/AQP4) is plotted against the rAb concentration. Solid circles indicate the EC_{50} for CDC. (E) Lateral and top views of an AQP4 tetramer. Extracellular loops A, C, and E are colored red, green, and blue, respectively. Loop C amino acids His151 and Leu154 are colored purple; membrane-spanning and intracellular amino acids are colored gray. (F and G) Binding of AQP4 rAbs to U87MG cells expressing M23-AQP4 (solid line) or M23-AQP4^{H151A/L154A} is shown as the ratio of bound rAb to cell-surface AQP4 (rAb/AQP4) (mean \pm SEM; $n = 3$). Data were fitted using a single-site total binding model. hC, human complement.

from individual NMO patients to test whether multimeric IgG plasma membrane assembly governs AQP4-IgG-mediated CDC in NMO. We identified a group of AQP4 rAbs with a distinct epitope specificity that displayed enhanced CDC on target cells expressing AQP4 OAPs. We observed that CDC was dependent on plasma membrane assembly of multimeric AQP4-IgG complexes, and antibody mutations that enhanced the interaction of membrane-bound AQP4-IgGs accentuated C1q activation. The results establish a framework for understanding and potentially treating pathologic antibody-mediated autoimmunity.

Results

AQP4 rAbs display discrete levels of classical complement activity. We first evaluated the contribution of the classical, alternative, and lectin pathways to AQP4-IgG-mediated CDC in vitro (Figure 1A). Chinese hamster ovary (CHO) cells expressing the M23-AQP4 isoform were incubated with the AQP4 rAb ON 07-5 no. 58 and com-

plete or depleted normal human serum (NHS) as a source of complement. We found that CDC in M23-AQP4 CHO cells was completely dependent on classical pathway activation. We observed no lysis with C1q-depleted serum, and CDC was rescued following the addition of recombinant C1q. In contrast, inhibition of the alternative or lectin pathway through the selective depletion of either complement factor B or mannose-binding lectin had no significant effect on CDC in this assay. CDC was not observed when only the lectin pathway was active (factor D and C1q depletion).

Next, we examined the ability of AQP4 rAbs with distinct binding affinities and epitope specificities (19) to activate CDC on M23-AQP4 OAPs (Table 1). The EC_{50} for CDC varied widely across AQP4 rAbs (3.2–1226 nM; Figure 1B and Table 1) and did not correlate with the levels of bound C1q or rAb (Figure 1, C and D, and Table 1). Interestingly, 4 rAbs (ON 09-3 no. 33, ON 07-5 no. 93, ON 10-1 no. 153, and ON 07-5 no. 186) activated CDC efficiently at low levels of bound C1q and rAb (Figure 1, C and D, and Table 1). This group of rAbs shared unique epitope sensitivity to the amino acids His151 and Leu154 in extracellular loop C (Figure 1, E and F) (19). In contrast, AQP4 rAbs insensitive to alanine substitutions at these positions (ON 07-5 no. 53, ON 07-5 no. 58, and ON 10-1 no. 121) (Figure 1G) showed higher levels of bound C1q and rAb at their EC_{50} for CDC (Figure 1, C and D, and Table 1).

His151 and Leu154 epitopes facilitate

AQP4-IgG Fc domain interactions on AQP4 OAPs. The IgG1 Fc fragment contains a CH2 domain that binds the C1q globular head and a CH3 domain that possesses a large hydrophobic patch critical for noncovalent interactions with neighboring IgG Fc domains (Figure 2A). His151/Leu154-dependent AQP4 rAbs may display enhanced CDC on M23-AQP4 OAPs by either optimizing Fc CH2 domain exposure or facilitating the interaction of neighboring OAP-bound AQP4-IgG. To test the relative contribution of these interactions to CDC, we introduced Fc domain point mutations that either increased (G236A/S267E/H268F/S324T/I332E, abbreviated as AEFTE) or decreased (K322A) CH2-C1q affinity (29), or promoted (E345R) or inhibited (I253D) CH3 Fc-Fc interactions (Figure 2B) (25). The Fc mutations did not impact rAb-binding affinity (Supplemental Table 1; supplemental material available online with this article; <https://doi.org/10.1172/JCI122942DS1>), but distinctly impacted CDC and C1q binding based on AQP4 rAb His151 and Leu154 epitope specificity (Supplemental Table 2).

Table 1. Summary of AQP4 rAb binding and CDC

AQP4 rAb	Loop epitopes	H151/L154 dependence	rAb K_D M23-AQP4 (nM)			rAb B_{max} M23-AQP4			CDC EC_{50} (nM)			C1q/AQP4 at EC_{50}	rAb/AQP4 at EC_{50}	Mean ASA score
			Mean	SEM	<i>n</i>	Mean	SEM	<i>n</i>	Mean	SEM	<i>n</i>			
ON 07-5 no. 186	A, C, E	Yes	15.2	2.4	13	1.0	0.1	13	3.2	1.1	5	5.2	17	2.9
ON 09-3 no. 33	A, C, E	Yes	24.7	3.6	3	0.6	0.1	3	10.8	3.8	5	5.9	26	-
ON 10-1 no. 153	C, E	Yes	195.0	46.1	7	0.9	0.1	3	23.6	3.2	3	4.6	16	3.3
ON 07-5 no. 93	A, C, E	Yes	16.9	3.1	5	1.1	0.1	5	10.9	1.3	5	7.7	11	-
ON 07-5 no. 53	C, E	No	14.8	2.4	15	1.0	-	-	20.1	5.3	6	10.5	44	2.4
ON 07-5 no. 58	A, C, E	No	61.3	8.3	10	1.2	0.2	6	51.4	9.9	7	8.7	38	2.7
ON 10-1 no. 121	A, C, E	No	2563.0	77.0	2	0.8	0.3	2	1226.1	199.3	2	-	-	-

Loop epitopes A, C, and E represent the extracellular loops containing unique amino acid epitope contacts as mapped by Owens et al. (19). His151/Leu154 dependence is the binding dependence to the unique extracellular loop C amino acids His151 and Leu154. The K_D value indicates the equilibrium dissociation constant for rAb binding to AQP4. B_{max} denotes the maximum number of binding sites at saturating antibody concentrations. EC_{50} denotes the effective concentration at which 50% cell lysis occurred by CDC using 5% human complement. C1q/AQP4 indicates the ratio of C1q fluorescence intensity over total AQP4 fluorescence intensity. rAb/AQP4 indicates the ratio of rAb fluorescence intensity over total AQP4 fluorescence intensity. The mean ASA score denotes the potential for multivalent C1q contacts quantified from super-resolution images as described by Soltys et al. (32).

The differing effects of CH2 and CH3 domain mutations are exemplified by His151/Leu154-independent and -dependent rAbs ON 07-5 no. 53 (Figure 2C) and ON 07-5 no. 186 (Figure 2F), respectively. Both IgG1 rAbs bind to AQP4 with similar affinity, however the His151/Leu154-dependent rAb ON 07-5 no. 186 activates CDC at a 6-fold lower CDC EC_{50} (ON07-5 no. 186: 3.2 nM vs. ON07-5 no. 53: 20.1 nM) (Table 1). For ON 07-5 no. 53, enhancing C1q-CH2 affinity (AEFTE) modestly increased the CDC EC_{50} to 9.3 nM (Figure 2C), whereas enhancing CH3 Fc-Fc interaction (E345R) increased the CDC EC_{50} to 4.1 nM, which was comparable to CDC by native ON 07-5 no. 186 (Figure 2, C and F, and Supplemental Table 2). CDC by native ON 07-5 no. 186 was insensitive to both the AEFTE and E345R mutations, indicating that binding of the rAb to its unique epitope had optimized CDC (Figure 2F). Importantly, both rAbs required Fc-Fc interaction to activate CDC, as the disrupting mutation I253D abolished CDC (Figure 2, C and F). Increasing C1q-CH2 affinity did not rescue or boost ON 07-5 no. 53 CDC when combined with mutations abolishing or enhancing CH3 Fc-Fc interactions (Figure 2C; I253D/AEFTE and E345R/AEFTE).

We further examined the role of CH3 domain interactions in driving CDC on M23-AQP4 OAPs using additional His151/Leu154-dependent and -independent AQP4 rAbs. The I253D mutation abrogated CDC activity in all AQP4 rAbs assayed, and this was independent of epitope specificity. The enhancing CH3 domain mutation E345R substantially increased CDC activity in His151/Leu154-independent rAbs (Figure 2, C-E). For example, CDC activity induced by ON 07-5 no. 58-E345R was fully rescued to reach the CDC levels seen with ON 07-5 no. 186-IgG1 (Figure 2D). In contrast, promoting Fc interaction had mixed effects on His151/Leu154-dependent rAbs (Figure 2, F-I). For example, CDC induced by ON 07-5 no. 93 was not affected by the E345R mutation (Figure 2G). The rAbs ON 10-1 no. 153-E345R and ON 09-3 no. 33-E345R showed some enhancement of CDC EC_{50} (ON 10-1 no. 153: 16.6 to 6.2 nM, ON 09-3 no. 33: 10.8 to 3.8 nM) (Figure 2, H and I), which could be due in part to the otherwise relatively low levels of C1q binding exhibited by these rAbs when

compared with other His151/Leu154-dependent rAbs. C1q binding increased markedly with the introduction of the E345R mutation (Figure 2, H and I).

While enhanced CH3 Fc-Fc interaction routinely increased C1q binding, it additionally promoted C1q activation. When compared with His151/Leu154-independent rAb ON 07-5 no. 53, the CDC EC_{50} for His151/Leu154-dependent rAb ON 07-5 no. 186 occurred at lower total levels of bound C1q (5.2 vs. 10.5 nM, respectively) and a lower percentage of C1q (C1q/AQP4 B_{max}) (5.8% vs. 53.6%, respectively) (Supplemental Table 2). Large increases in C1q binding did not enhance CDC activated by ON 07-5 no. 186 (Figure 2D; AEFTE and E345R), and ON 07-5 no. 53-E345R dramatically increased CDC, despite a minimal boost in C1q binding compared with 07-5 no. 53-AEFTE (Figure 2C). Like ON 07-5 no. 186, strengthening the Fc-Fc interactions of His151/Leu154-dependent rAb ON 07-5 no. 93 (E345R) increased C1q binding, without enhancing CDC (Figure 2G).

Disruption of CH3 Fc-Fc interaction (I253D) or interference with CH2 domain C1q binding (K322A) eliminated C1q binding and CDC for both His151/Leu154-dependent ON 07-5 no. 53 and His151/Leu154-independent ON 09-3 no. 33 (Figure 2, C and I). Enhancement of CH2 domain C1q binding (AEFTE) was not able to restore C1q binding or CDC when introduced in combination with the I253D mutation for rAbs ON 07-5 no. 53 and ON 07-5 no. 186 (Figure 2, C and F). Consistent with a role for CH3 Fc-Fc interaction in C1q activation, rAb ON 09-3 no. 33-AEFTE/I253D bound similar levels of C1q to native rAb but failed to initiate CDC. Hence, epitope-mediated CH3-driven Fc-Fc interactions enhance both C1q binding and activation.

Enhancement of CH2-C1q binding or CH3-Fc interactions fails to rescue CDC on M1-AQP4. Previous work demonstrated that AQP4 rAbs and polyclonal serum AQP4-IgG are unable or have limited abilities to initiate CDC on M1-AQP4 (12, 17). Compared with densely packed M23-AQP4 tetramers in OAPs, M1-AQP4 tetramers are dispersed throughout the cell membrane (30, 31), resulting in greater challenges for IgG complex assembly, C1q binding, and activation (Figure 3A). Neither His151/Leu154-dependent

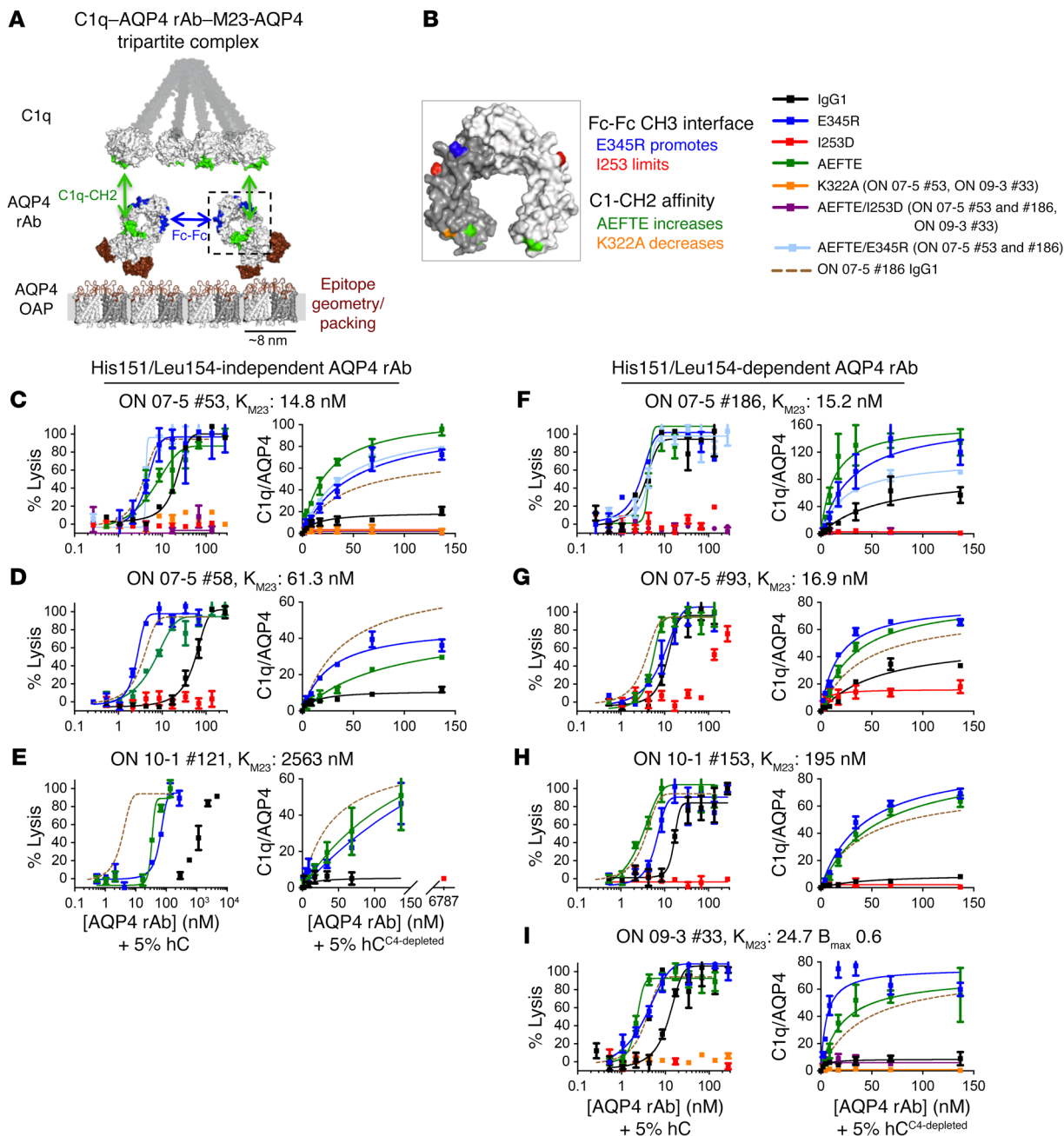


Figure 2. Impact of CH2-C1q affinity and CH3 Fc-Fc interactions on AQP4-IgG-mediated CDC. (A) Space-filling and ribbon models of C1q, AQP4 rAb, and M23-AQP4 OAPs illustrating potential interactions driving C1q–AQP4 rAb–M23-AQP4 multivalent complex assembly. C1q globular heads bind to the CH2 domain of AQP4 rAb (green), while neighboring AQP4 rAbs interact via CH3 hydrophobic patches (blue). Fab variable regions and AQP4 extracellular loops are colored brown. (B) Space-filling model of the Fc region of a divalent AQP4 rAb (boxed area from A) denoting residues with engineered mutations to promote (green, blue) or limit (orange, red) C1q-CH2 or CH3-CH3 interactions. AEFTE denotes the combination G236A/S267E/H268E/S324T/I332E Fc domain mutations. CDC (left graphs; mean \pm SEM; $n = 4$) and C1q binding (right graphs; mean \pm SD; $n = 3$) were measured for His151/Leu154-independent (C–E) and His151/Leu154-dependent (F–I) AQP4 rAbs. rAb binding affinity on M23-AQP4 (K_{M23}) is displayed in the top left corner of each CDC graph. The CDC and C1q binding curves for rAb ON 07-5 no. 186 (dotted brown line) is displayed in each graph for comparison. The K322A, AEFTE/I253D, and AEFTE/E345R mutations were introduced into select rAbs as indicated in the key.

nor His151/Leu154-independent AQP4 rAbs showed significant CDC on cells expressing M1-AQP4 (Figure 3, B–H). Enhancement of Fc-Fc interactions (E345R) or CH2-C1q binding (AEFTE) did not rescue CDC. In addition, the combined mutation (AEFTE and E345R) failed to restore CDC on M1-AQP4 (Figure 3, B and E). ON 07-5 no. 58-E345R, which binds with equal affinity to M1-AQP4

and M23-AQP4 (12), was the only rAb to show minimal CDC on M1-AQP4, although activity was severely limited (Figure 3C).

We next examined C1q binding on AQP4 rAbs bound to M1-AQP4. All AQP4-IgG1 rAbs showed reduced C1q binding when compared with M23-AQP4 (Figure 3 and Figure 2). Despite generally lower levels of bound C1q, higher concentrations of the

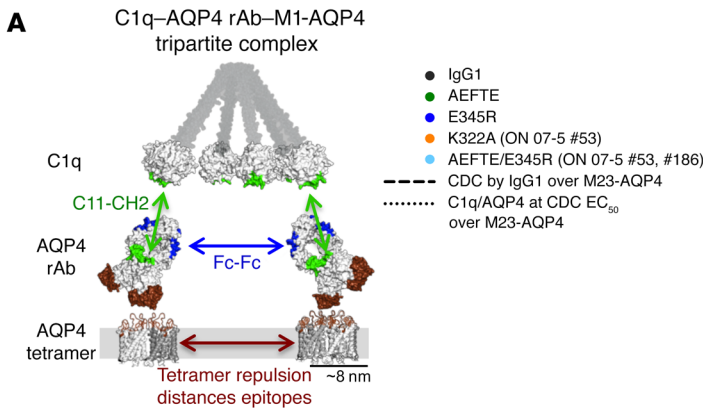
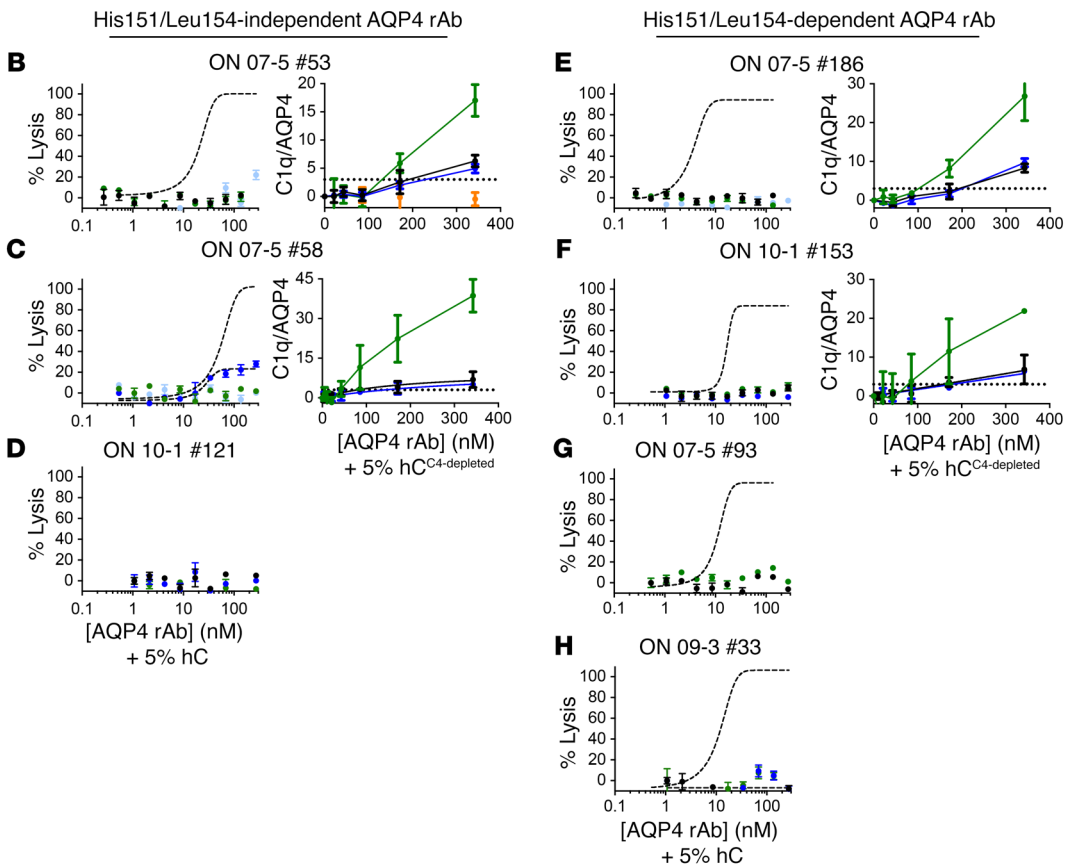


Figure 3. AQP4 rAb CDC and C1q binding on M1-AQP4. (A) Space-filling and ribbon models of C1q, AQP4 rAb, and M1-AQP4 tetramers illustrating interactions potentially driving C1q-AQP4 rAb-M1-AQP4 multivalent complex assembly. C1q globular heads bind to the CH2 domain of AQP4 rAb (green), while neighboring AQP4 rAbs interact via CH3 hydrophobic patches (blue). Fab variable regions and AQP4 extracellular loops are colored brown. (B) CDC (left graphs; mean \pm SEM; $n = 4$) and C1q binding (right graphs; mean \pm SD; $n = 3$) was measured on M1-AQP4-expressing CHO cells using His151/Leu154-independent (B-D) and His151/Leu154-dependent (E-H) AQP4 rAbs. CDC activity for the native IgG1 AQP4 rAb on M23-AQP4 is plotted as the dotted black line. Some Fc domain mutations were introduced only into selected rAbs, as indicated in the key.



His151/Leu154-dependent rAbs ON 07-5 no. 186-IgG1 and ON 10-1 no. 153-IgG1 bound C1q at levels that were sufficient to reach 50% cytotoxicity on M23-AQP4 (Figure 3, E and F, and Supplemental Table 3), yet yielded no CDC on M1-AQP4. Furthermore, ON 07-5 no. 53-AEFTE and ON 07-5 no. 58-AEFTE bound sufficient levels of C1q on M1-AQP4 for classical complement pathway activation on M23-AQP4 but also failed to induce CDC (Figure 3, B and C). Last, and in contrast to the observed C1q-binding effect on M23-AQP4, the CH3 domain E345R mutation did not enhance C1q binding on M1-AQP4 tetramers (Figure 3, B, C, E, and F).

The results suggest that the lack of AQP4 OAP formation by M1 tetramers prevents CH3 domain Fc-Fc interactions that are necessary for C1q activation. To evaluate this question directly, we probed for sublytic complement activation on target cells (C3d deposition) using C5-depleted serum. We did not detect C3d deposition on cells expressing M1-AQP4 for any AQP4-specific or iso-

type control IgG1 rAb assayed (Figure 4A). For instance, ON 07-5 no. 58 showed significant C3d deposition on M23-AQP4 but not on M1-AQP4 at an identical rAb concentration (Figure 4, A and B). For some rAbs (ON 07-5 no. 58, ON 07-5 no. 186, and ON 10-1 no. 153), AEFTE and ER mutations modestly increased C3d deposition on M1-AQP4 cells but failed to initiate CDC (Figure 4A and Figure 3). Sublytic activation was dependent on CH3 Fc-Fc interaction, as the combination AEFTE-I253D mutations inhibited activation (Figure 4A, AEFTE-I253D). Consistent with partial CDC on M1-AQP4, ON 07-5 no. 58-E345R produced the highest levels of C3d deposition, which approached, but did not equal, the level of deposition compared with that seen on M23-AQP4 cells (Figure 4B).

AQP4 rAb-mediated CDC correlates with IgG clustering on super-resolution microscopy. The accumulated data support a critical role for Fc-Fc-driven antibody clustering in AQP4-IgG-mediated CDC. We next used super-resolution microscopy to

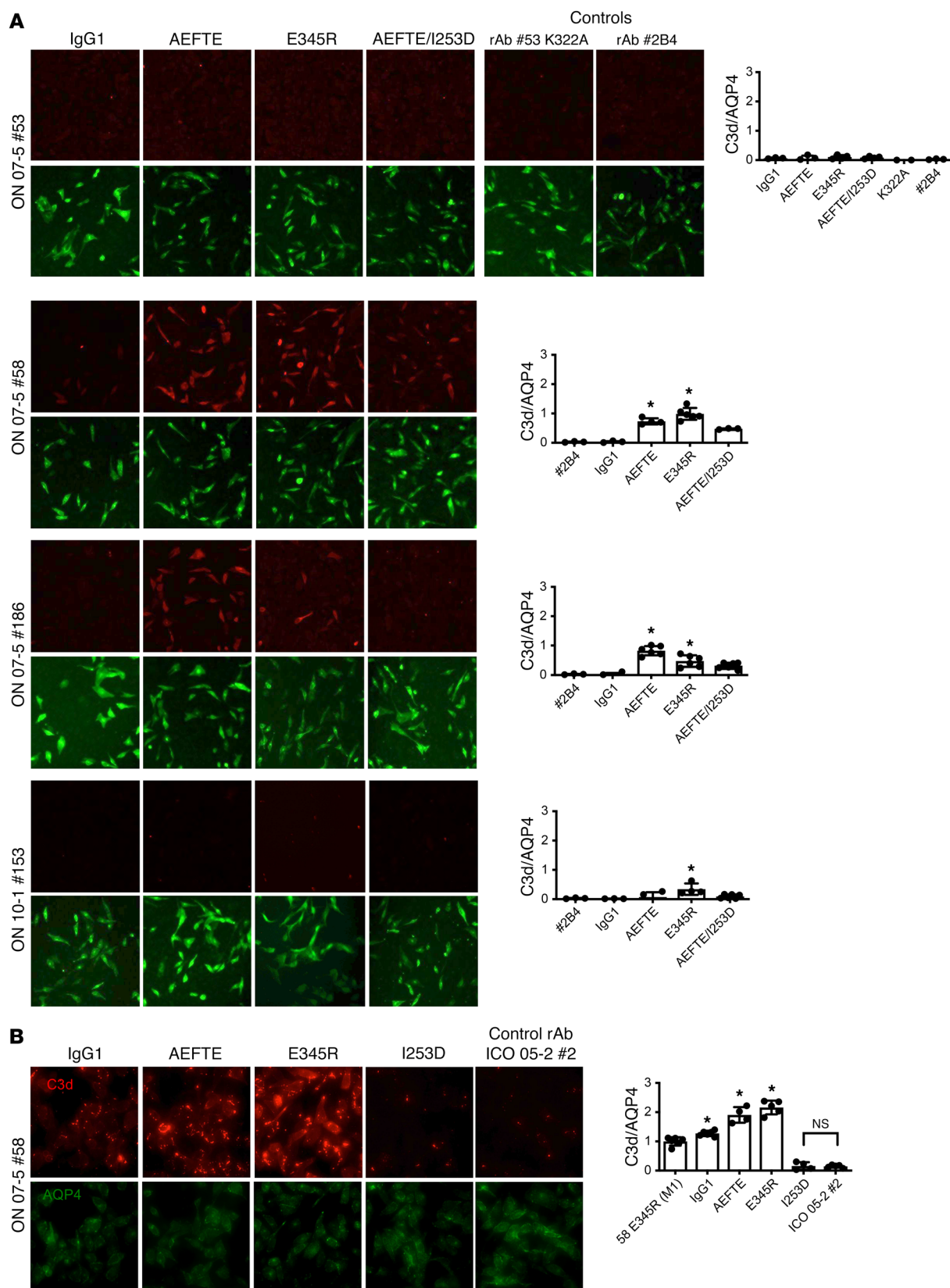


Figure 4. Complement deposition on M1-AQP4 and M23-AQP4-expressing CHO cells. Complement protein deposition on M1-AQP4-expressing (A) and M23-AQP4-expressing (B) CHO cells was detected by C3d immunostaining. AQP4 and control rAbs were as shown. The fluorescence intensity of C3d/AQP4 is tabulated with each point representing a single image, mean \pm SD on bars. $*P < 0.05$, by 1-sided ANOVA with Tukey's post hoc test compared with IgG1 or AEFTE/I253D (A) or ON 07-5 no. 58 E345R (B). C3d deposition by all IgG1 rAbs did not differ from that by control rAb 2B4 on M1-AQP4. Original magnification, $\times 400$.

test whether differences in AQP4 rAb clustering on M23-AQP4 could be directly correlated with enhanced complement activation. We recently developed an image-processing algorithm to quantify the average size and spatial arrangement of AQP4 rAb clusters on AQP4 OAPs at less than 30-nm resolution using stimulated emission depletion (STED) microscopy (Figure 5A) (32). Using this method, we evaluated the average resolvable antibody cluster spread for multiple AQP4 rAbs on M23-AQP4 OAPs. His151/Leu154-dependent rAbs bound to M23-AQP4 OAPs generally appeared as larger clusters when compared with His151/Leu154-independent rAbs, independent of binding affinity (Figure 5B). As predicted, promoting antibody clustering via the E345R CH3 domain mutation significantly increased the average cluster size of His151/Leu154-independent AQP4 rAbs to a degree comparable to that seen with His151/Leu154-dependent AQP4 rAbs (Figure 5B).

We used a previously validated antibody spatial arrangement (ASA) scoring method to quantitate the multivalent C1q-binding potential of AQP4 rAbs by STED microscopy (32). An ASA score of 1 represents a low probability for multivalent C1q binding, while a score of 4 represents a high probability (Figure 5C). Nonbiased hierarchical clustering analysis demonstrated that ASA scores for His151/Leu154-dependent AQP4 rAbs and AQP4 rAbs with enhanced Fc-Fc interaction (E345R mutation) were skewed higher (Figure 5D). ASA scores were largely independent of AQP4 rAb concentration, indicating that AQP4 antibody clustering on M23-AQP4 OAPs was driven predominantly by the intrinsic binding properties of the rAb. Indeed, AQP4 rAbs with higher mean ASA scores demonstrated lower AQP4 antibody saturation and C1q binding at EC_{50} (Figure 5, E and F, and Table 1). Thus, data from super-resolution STED microscopy support a model of complement activation in NMO that is driven by the surface assembly of multimeric AQP4-IgG clusters.

Antibody clustering drives CDC on primary murine astrocytes. We examined whether the factors driving CDC on M23-AQP4-transfected cells were reproduced on primary murine cerebellar and cortical astrocyte cultures. Consistent with data derived from M23-AQP4-transfected cells, rAb ON 07-5 no. 186 demonstrated greater maximal CDC than did ON 07-5 no. 53 on both astrocyte populations ($P < 0.05$, unpaired Student's t test) (Figure 6A and Supplemental Videos 1-3). Furthermore, enhancement of C1q binding (AEFTE mutation) did not increase CDC for either AQP4 rAb (Figure 6B); however, promotion of Fc-Fc interaction (E345R mutation) accentuated CDC activated by ON 07-5 no. 53 to levels comparable to those for native ON 07-5 no. 186 (Supplemental Video 4). As anticipated, the I253D mutation that inhibited Fc-Fc interaction abolished CDC induced by ON 07-5 no. 53.

Both AQP4 rAbs activated CDC at enhanced levels on cerebellar astrocytes compared with cortical astrocytes (Figure 6A and Supplemental Videos 2 and 5). To investigate whether this difference correlated with regional variations in AQP4 protein expression, we quantified AQP4 OAP abundance and array size using super-resolution stochastic optical reconstruction (STORM) microscopy (Figure 6, C-E). Consistent with prior studies (33, 34), cerebellar astrocytes expressed both higher levels of AQP4 protein (Figure 6F; $P < 0.05$, Student's t test) and organized AQP4 into larger OAPs (Figure 6G; $P < 0.0001$, Kolmogorov-Smirnov test).

Antibody clustering drives pathologic complement activation by polyclonal serum from patients. Given the critical role for CH3 Fc-Fc interactions in organizing AQP4 rAb clusters, we asked whether it was possible to destabilize CH3 domain self-assembly by AQP4 rAb and polyclonal NMO serum using a small peptide, Fc-CH3, which binds human Ig Fc with high affinity and inhibits CDC induced by monoclonal anti-CD20 and anti-CD38 antibodies (25, 35). The peptide inhibited CDC by both His151/Leu154-independent (Figure 7A) and -dependent (Figure 7B) AQP4 rAbs, and the inhibition was not overcome by the Fc mutations (AEFTE) that optimized C1q binding.

We next tested whether Fc-CH3 peptide could inhibit CDC driven by patients' polyclonal NMO serum. Polyclonal serum from 7 distinct relapsing patients had variable levels of CDC on target cells expressing M23-AQP4 (Figure 7C) (18). CH3-Fc peptide consistently reduced complement injury when compared with control peptide ($P < 0.05$, paired Student's t test) (Figure 6C). The results indicate that antibody clustering drives pathologic complement activation by polyclonal NMO serum IgG and that inhibition of CH3 domain-mediated IgG multimerization may provide a therapeutic approach for treating NMO attacks.

Discussion

We examined the molecular interactions driving classical complement activation by pathogenic AQP4 autoantibodies in NMO. Using recombinant monoclonal anti-AQP4 antibodies derived from patients with NMO, we demonstrate that CH3 Fc-Fc-mediated assembly of multimeric autoantibody complexes on plasma membrane arrays of AQP4 protein is critical for C1q activation (Figure 8A). As predicted, large M23-AQP4 OAPs provide a stable, high-affinity platform for AQP4-IgG binding, complex assembly, C1q engagement, and C1q activation (16, 17, 22, 36, 37) (Figure 8A). In contrast, mobile M1-AQP4 tetramers resist array assembly and prevent the formation of Fc-Fc interactions between bound AQP4 autoantibodies (Figure 8A, left). AQP4-IgG binding affinity, epitope specificity, and titers combine to determine the distribution and orientation of autoantibodies on the surface of target astrocytes. High- or low-affinity AQP4 autoantibodies with His151/Leu154-dependent epitope specificity orient and self-assemble into clusters that are stabilized by adjacent CH3-CH3 binding, permitting efficient C1q binding and activation despite relatively low levels of bound IgG (Figure 8A, top). His151/Leu154-independent autoantibodies, however, require higher levels of IgG binding to assemble IgG platforms sufficient for C1q binding and activation (Figure 8A, bottom). Consequently, the severity and distribution of CNS NMO lesions are probably dependent on the combined action of factors affecting AQP4 OAP formation, AQP4-IgG binding, and activation of the complement pathway (Figure 8B). Future studies of the role of these individual mechanisms may facilitate the development of novel diagnostic, prognostic, and therapeutic strategies to predict and treat disease relapses.

Classical pathway-dependent cytotoxicity initiates with multivalent C1q-IgG binding to IgG clusters, resulting in C1 enzymatic activation, downstream proteolytic cascade activation, and deposition of membrane attack complexes on target cells. The molecular mechanisms regulating C1 activation have been the subject of considerable investigation (24, 38). C1 activation requires mechan-

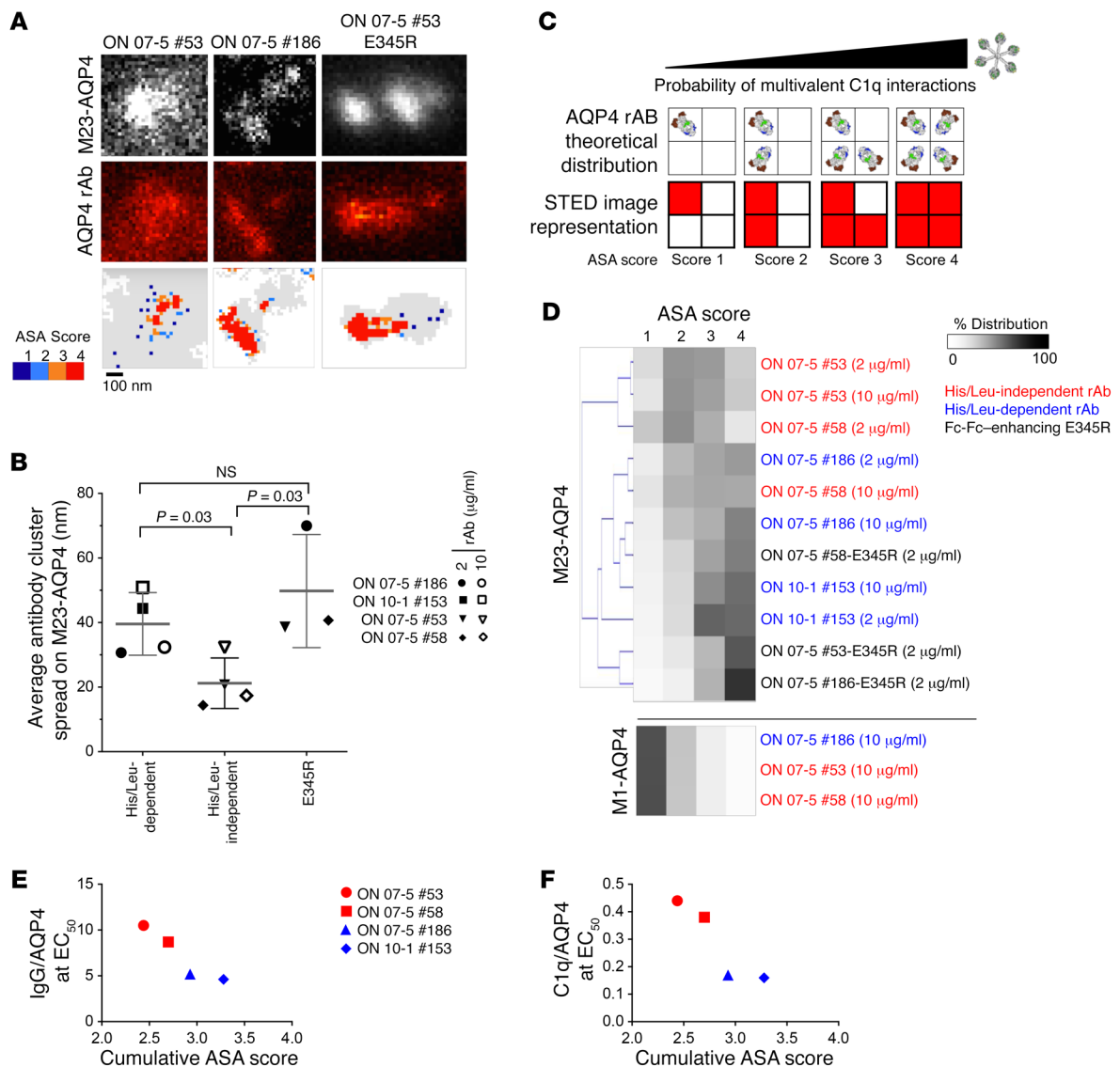


Figure 5. Super-resolution microscopy of membrane-bound AQP4 rAb clustering on M23-AQP4 OAPs. (A) Representative images showing M23-AQP4 and AQP4 rAb and ASA scores. Image scale: pixel = 19.5 × 19.5 nm; scale bar: 100 nm. (B) The magnitude of cluster spread for the average resolvable rAb cluster was grouped by epitope-binding dependence and compared using ANOVA with Tukey’s test for multiple comparisons. Each data point represents the mean from at least 3 images throughout. (C) Theoretical depiction of the ASA scoring scale. A hypothetical antibody distribution is displayed schematically to illustrate the relative size of AQP4 rAb and the image pixel. Pixel groups containing a higher concentration of rAb signal (bottom) are considered to have a higher probability of clustering and forming multivalent contacts with C1q. (D) A hierarchical clustering analysis of ASA scores was performed for His151/Leu154-independent rAbs (red), His151/Leu154-dependent rAbs (blue), and E345R Fc-mutated rAbs (black) on CHO cells expressing M23-AQP4 and M1-AQP4. The mean ASA score is plotted against levels of (E) bound rAb and (F) C1q at CDC EC₅₀.

ical stress to disrupt the C1r2:C1s2 complex housed within the C1 collagenous stems (23, 39). The activation energy necessary to achieve this stress may be minimized by the pattern of engagement between C1q and membrane-bound AQP4-IgG. In NMO, AQP4 rAbs that efficiently cluster on M23-AQP4 OAPs, either through optimally arrayed epitopes (His151/Leu154-dependent AQP4 rAbs) or enhanced CH3 Fc-Fc interaction, activate C1q efficiently, despite low levels of bound protein, by optimizing the spatial interaction between the hexameric C1q and IgG Fc CH2 domains. In contrast, AQP4 rAbs on M1-AQP4 fail to coalesce into the necessary arrangement to activate the complement cascade, despite binding sufficient levels of C1q. IgG hexamer assemblies may represent a

best-fit platform that both optimizes high-affinity C1q binding and minimizes the activation energy needed to disrupt the C1r2:C1s2 complex. Indeed, IgG hexamers induce fluid-phase complement activation in the absence of target antigen (25, 26, 40). As only a limited number of C1q globular heads may need to contact a hexamer to initiate activation, it is possible that nonhexamer platforms arrayed on M23-AQP4 OAPs may be suitable for CDC.

Using STED microscopy, we visualized distinct spatial arrangements of plasma membrane-bound AQP4-IgG that varied depending on epitope specificity (Figure 5). While a hexameric organization may represent the optimal structure for C1q binding and activation, the geometry of certain epitopes on M23-

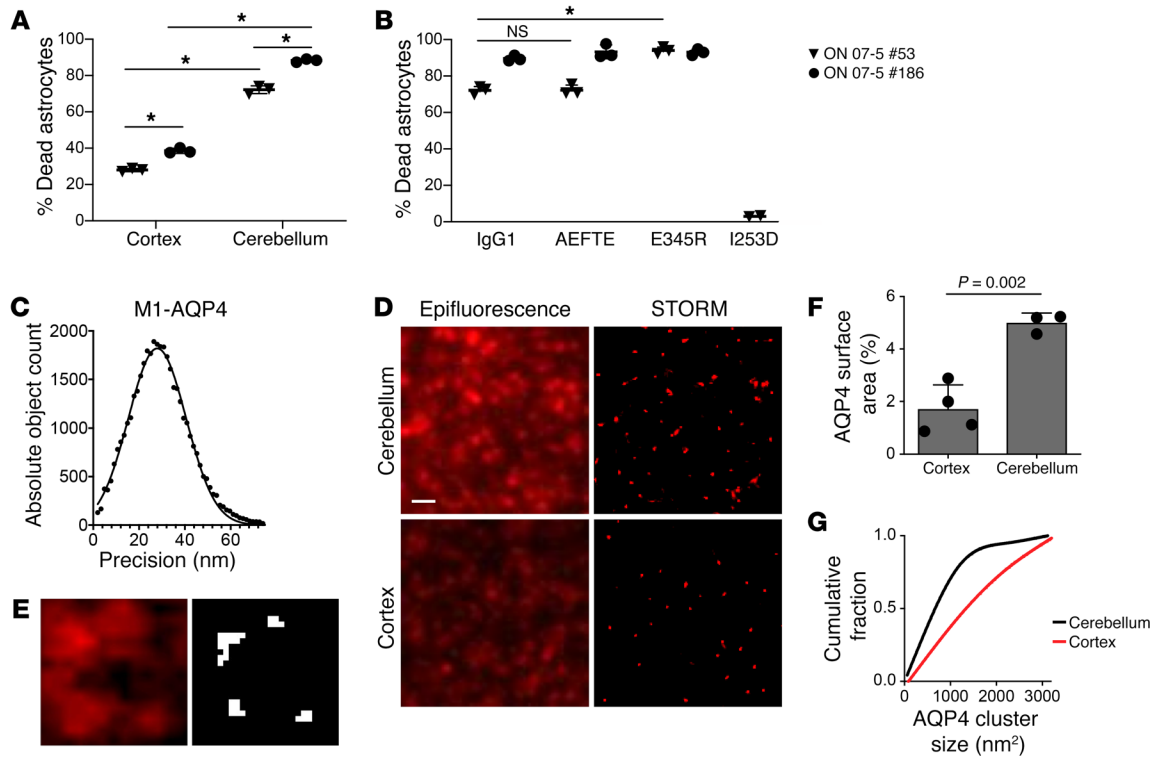


Figure 6. AQP4 rAb CDC and AQP4 expression in primary astrocyte cultures. (A and B) Cultures of purified primary astrocytes from murine cortex or cerebellum were treated with 20 $\mu\text{g}/\text{ml}$ AQP4 rAb with 5% human complement for 6 hours. The percentage of dead astrocytes was quantified as DRAQ7⁺ cells over the total cell count (adjusted $*P < 0.05$, by 1-sided ANOVA with Tukey's post hoc test. Each data point represents a single-well mean of 4 to 9 images). (A) CDC induced by native IgG1. (B) CDC induced by the indicated mutant Fc domains in primary cerebellar astrocytes. (C–G) Super-resolution STORM imaging of AQP4 expression. (C) Alexa Fluor 647 fluorophore resolution was quantified over M1-AQP4-transfected CHO cells ($n = 5$ images). (D) Low-magnification epifluorescence and STORM images demonstrating resolution enhancement of cerebellar and cortical cultures. Scale bar: 1000 nm. (E) High-magnification images of cerebellar culture showing an epifluorescence image (left) and the corresponding binary threshold image used to quantify AQP4 expression (right). (F) Quantification of AQP4 expression as a percentage of the total cell-surface area ($P = 0.002$, by t test. Each data point represents a single image; data are shown as the mean \pm SD). (G) Quantification of AQP4 array size ($P < 0.0001$, by Kolmogorov-Smirnov test; $n = 5$ images per group).

AQP4 OAPs may restrict the assembly of certain AQP4-IgGs. In addition, the orientation of bound AQP4-IgG CH2 domains may impact C1q binding, as evidenced by the variations in C1q binding to native and mutagenized Fc domains on M1-AQP4 (Figure 3). Thus, the clusters of AQP4 rAb visualized on M23-AQP4 OAPs represent geometric variations of idealized IgG hexamers that drive C1q binding and subsequent activation. In patients with NMO, polyclonal serum AQP4-IgG binds to distinct epitopes on target OAPs using CH3 domain interactions to optimize C1q binding and activation despite constraints imposed by steric interference and competing Fc domain interactions (Figure 8B). Recently, Tradtrantip and colleagues (28) demonstrated that preformed, fluid-phase IgG hexamers limit experimental NMO lesion formation *ex vivo* and *in vivo*. Fluid-phase IgG hexamers do not bind AQP4 or cell membrane proteins but rather inhibit C1q binding and competing Fc domain interactions (Figure 8B). It is likely that these artificially assembled IgG platforms provide idealized targets for C1q that outcompete imperfect AQP4-IgG multimers assembled on AQP4 OAPs.

In NMO, there is a predilection for optic nerve and spinal cord injury. In the optic nerve and spinal cord, AQP4 is expressed and assembled into large OAPs (41, 42). This may allow surface AQP4-IgG assembly and complement activation to overwhelm local tissue complement inhibition (Figure 8B). In NMO, pathology is also

notably absent in peripheral organs despite significant AQP4 OAP expression (43), AQP4-IgG binding (44), and tissue susceptibility to complement activation. For example, the kidney is particularly susceptible to an array of complement-mediated disorders but is spared in NMO despite high levels of AQP4 expression (45, 46). While the local expression of complement inhibitors probably plays a role in elevating the threshold level for C1q activation and membrane attack complex deposition (47, 48), AQP4 OAP size, number, and organization also affect the initiation of the classical complement pathway to influence the regional specificity of CDC activation and consequent tissue injury (Figure 6) (12, 49). Therefore, modulating AQP4 OAP array formation may offer a therapeutic strategy for minimizing injury during acute attacks (12, 50).

The importance of IgG assembly formation for complement activation may have clinical implications for other antibody-mediated autoimmune disorders. For example, in anti-NMDA receptor (anti-NMDAR) encephalitis, anti-NMDAR IgG1 antibodies induce prominent memory and behavioral deficits in the absence of tissue destruction. Complement activation is not observed in pathologic specimens, despite large amounts of IgG1 autoantibodies (51). Instead, anti-NMDAR antibodies induce rapid receptor internalization (52) that likely prevents CH3 domain Fc-Fc interactions between plasma membrane-bound anti-NMDAR

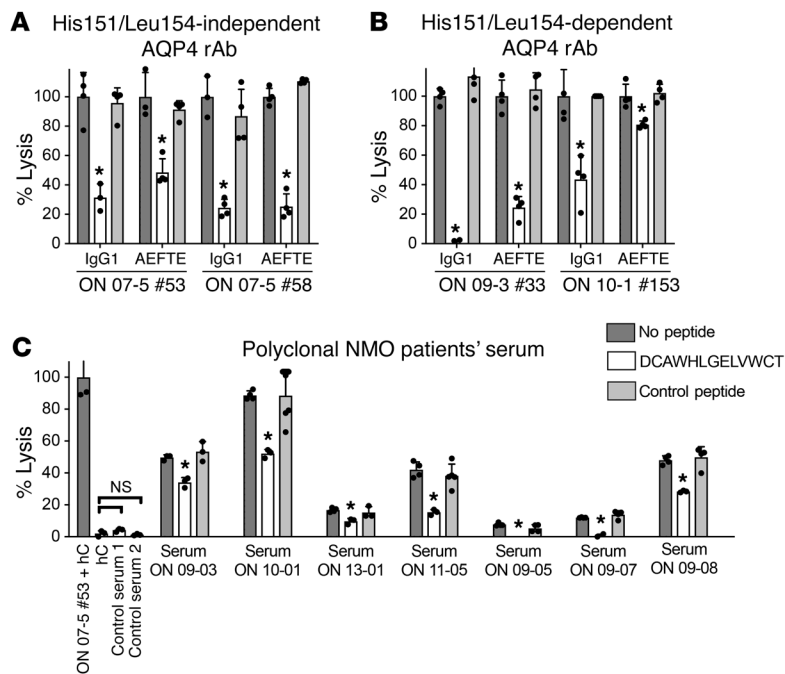


Figure 7. Fc-CH3 peptide inhibits CDC induced by AQP4 rAb and sera from NMO patients. CDC induced by His151/Leu154-independent AQP4 rAb (A), His151/Leu154-dependent AQP4 rAb (B), or sera from NMO patients (C) was measured by an LDH release assay in the presence or absence of Fc-CH3 or control peptide. Brackets denote lack of statistical significance. The peptide concentration was 40 μ M for all assays. Data were derived from a representative trial ($n = 3$ total trials, each of which had 4 experimental replicates). AEFTE denotes the combination Fc domain mutations that enhance C1q-antibody interaction. * $P < 0.05$, by paired *t* test.

IgG1. Conversely, in myasthenia gravis, autoantibodies against the nicotinic acetylcholine receptor (nAChR) bind monovalently and bivalently to dense, highly ordered hexagonal lattices at the neuromuscular junction (53). Although some autoantibodies may modulate nAChR signaling (54), complement activation is commonly observed in regions of anti-nAChR IgG deposition, and the destruction of neuromuscular junctions contributes to disease pathology (55). Indeed, the anti-C5 complement monoclonal antibody eculizumab was recently approved for the treatment of refractory myasthenia gravis (56). Large immobile arrays of target antigen may be the ideal target for complement-mediated humoral immunity, given the stable assembly of antibodies through the formation of CH3-CH3 interactions.

The requirement of ordered Fc domain organizations for complement activation by AQP4-IgG introduces unique challenges to correlating antibody titers with lesion severity and disease activity. First, as evidenced by His151/Leu154-independent and -dependent AQP4 rAbs, individual AQP4 autoantibodies may differ profoundly in their ability to activate complement. As a result, NMO patients' serum may activate complement with markedly different efficiencies despite similar autoantibody titers. Quantifying the specific titers of AQP4 autoantibody subpopulations and monitoring their access to the CNS may aid in predicting the frequency and severity of clinical attacks (57). Antibody glycosylation may further impact complement activation and result in dynamic fluctuations in antibody effector function despite stability in AQP4-IgG titers (58–60).

CH3 domain Fc-Fc interactions provide a target for complement inhibition in NMO and other autoimmune disorders. Current complement therapeutics targeting proteins such as C5 and C1q (6) carry significant risks for meningococcal infection (61) or kidney injury (62). More targeted inhibition of IgG CH3 Fc-Fc interactions should inhibit AQP4-IgG complement-mediated astrocyte destruction yet leave the alternative and lectin pathways intact. Our initial work demonstrates that CH3 domain peptides can block C1q activation in NMO patients' sera. Additional efforts to design small-molecule inhibitors with CNS penetration will be needed to advance this approach, as small peptides have limited CNS penetration and short in vivo half-lives. Alternatively, antibody mutations that limit Fc-Fc interactions may advance the design of competitive AQP4 monoclonal antibody-blocking antibodies (21).

In conclusion, we developed a molecular model for classical complement activation by AQP4 autoantibodies in NMO. The model explains the influence of AQP4-IgG epitope specificity and AQP4 OAP array assembly on autoantibody-mediated CDC and offers new avenues for monitoring disease activity and treating relapse. This model advances our understanding of the pathogenesis of antibody-mediated autoimmune disorders and highlights an approach for the design of next-generation complement therapeutics.

Methods

AQP4 rAbs. CSF plasmablasts isolated from clinically relapsing NMO patients were used to generate individual recombinant monoclonal AQP4 autoantibodies as described previously (10). Briefly, single-cell reverse transcriptase PCR was performed on isolated CD138⁺CD19⁻ CSF plasmablasts to amplify heavy- and light-chain variable regions, and the resulting cDNA was then cloned and cotransfected into HEK293 EBNA cells (American Type Culture Collection [ATCC]) to produce monoclonal antibodies. These rAbs were purified from culture supernatant using protein A columns, with structural and functional integrity confirmed by nondenaturing gel electrophoresis and immunohistochemistry.

The AQP4 rAbs used in this study were recovered from 3 AQP4 seropositive patients, and the extracellular loop amino acid epitope specificities are as described previously (26). Isotype control antibodies included rAb 2B4 (63), IC05-2 no. 2 (64), and rAb ON 07-5 no. 132 (non-AQP4 antibody).

Fc-domain point mutations that modulate the Fc-C1q (29) or Fc-Fc interface (25) were introduced into AQP4 rAbs by site-directed mutagenesis and confirmed by DNA sequencing. The AEFTE mutation increases C1q affinity, while the K322A mutation decreases C1q affinity. The E345R and I253D mutations, respectively, enhance and limit Fc-Fc interactions. Amino acid numbering follows the EU index in Kabat et al. (65).

NMO patients' serum, complement, and peptides. Serum was obtained from AQP4-IgG seropositive NMO patients and control AQP4-IgG seronegative NMO patients. Patients' serum was heat inactivated prior to use in CDC assays. All assays tested CDC activation by serum from an individual patient at a final concentration of 5%.

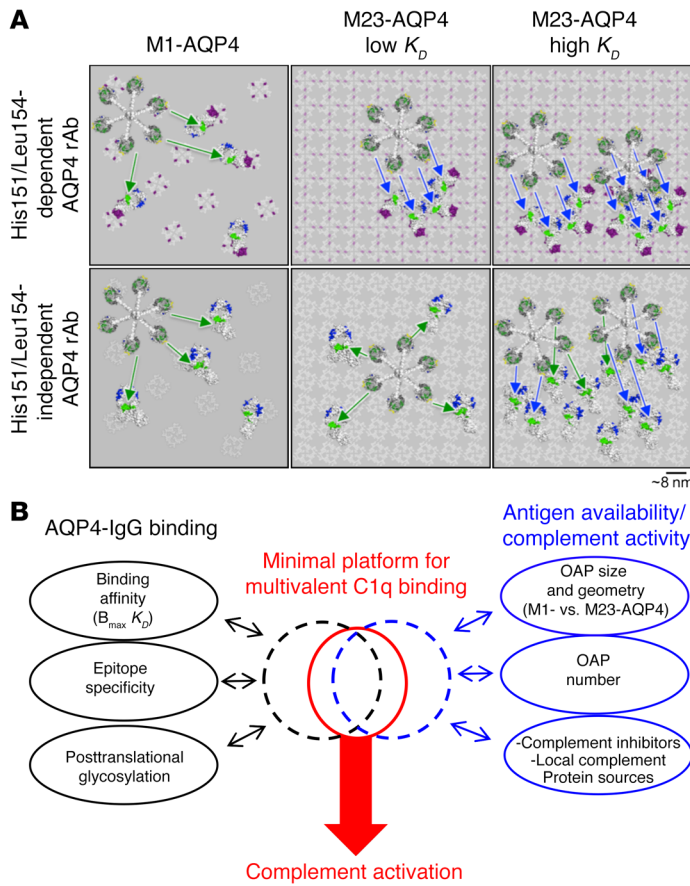


Figure 8. Model of classical pathway complement activation in NMO. (A) Space-filling models depicting the effect of His151/Leu154 epitope dependence for rAb clustering on M1-AQP4 and M23-AQP4. Some AQP4 rAb assemblies promote C1q binding without (green arrows) or with (blue arrows) subsequent activation. On M1-AQP4, C1q can access CH2-binding sites (green) but will not activate, as antibody-Fc interaction (blue) is limited by the repulsion of adjacent M1-AQP4 tetramers. On M23-AQP4 arrays, the Fc domain of His151/Leu154-dependent rAbs are oriented in a geometry that optimizes the formation of CH3 domain interactions (blue) between neighboring rAbs to create ideal platforms for C1q binding and activation. The spatial arrangements of His151/Leu154-independent AQP4 rAbs are not equally optimized and require higher levels of rAb binding to achieve optimal interaction between adjacent CH3 Fc-Fc domains (bottom). **(B)** List of antibody-intrinsic (left) and -extrinsic (right) factors affecting the assembly of IgG hexamers on membrane AQP4 tetramers and OAPs.

NHS and complement-depleted human serum were used as sources of human complement (Complement Technologies). MBL protein was depleted from NHS over a sepharose 4B column, with depletion confirmed by Western blotting. The Fc-CH3 (DCAWHLGELVWCT) (25, 33) and control (WHTPDSLRLNSGGGC) (66) peptides were synthesized by GenScript and MilliporeSigma, respectively.

Cell culture and reagents. All cells were incubated at 37°C in 5% CO₂. AQP4 expression was confirmed via immunohistochemistry. For assays with stable AQP4-expressing CHO cells (for rAbs) or U-87MG cells (for patients' serum), cells were plated at 37,500 and 52,500 cells/well, respectively, in tissue culture 96-well plates and incubated overnight in complete media as described below, with assays performed the following day. All cell lines, including HEK-EBNA cells for rAb production, were authenticated at the University of Colorado Cancer Center Monoclonal and Tissue Culture Core.

CHO cells expressing M1- or M23-AQP4 were provided by Alan Verkman (UCSF, San Francisco, California, USA) and cultured with G418 supplementation to maintain AQP4 expression (19). CHO cells were grown in F12 media supplemented with 10% FBS, 10 µg/ml streptomycin, 10 U/ml penicillin, and 0.25 µg/ml amphotericin B (all from Gibco, Thermo Fisher Scientific). U-87MG cell lines permanently expressing M23-AQP4 were cultured in MEMα media supplemented with 10% FBS, 1 nM sodium pyruvate, 1× nonessential amino acids, 10 µg/ml streptomycin, 10 U/ml penicillin, and 0.25 µg/ml amphotericin B.

A permanent cell line expressing M23-AQP4 with H151A and L154A mutations was generated for epitope mapping studies. Mutations were introduced into human M23-AQP4 using the GeneArt Site

Directed Mutagenesis Kit (Thermo Fisher Scientific, catalog A13282) and confirmed by DNA sequencing. The final construct (pcDNA3.1-M23AQP4 H151A L154A) was transfected into the U-87MG cells (ATCC, HTB-14) in a 6-well tissue culture dish using Lipofectamine 2000 (Thermo Fisher Scientific, catalog 11668027). Cells were incubated at 37°C with 5% CO₂ and selected using G418 (400 µg/ml). Clones were then individually diluted into single wells of a 96-well plate. Individual clones were screened for AQP4 expression and AQP4 rAb binding by immunohistochemistry. The WT M23-AQP4 U-87MG cell line was generated as previously described (19).

Primary pure murine astrocyte cultures were prepared from C57Bl6 pups as previously described with some modifications (67). Mixed glial cells were isolated from P1-3 dissociated cortex and cerebellum. Astrocytes were purified using the Anti-GLAST (ACSA-1) MicroBead Kit (Miltenyi Biotec) and plated in poly-D-lysine-coated 24- or 48-well plates. Cell population purity was greater than 95%, with AQP4 expression limited to astrocytes (67, 68-70). Experiments were performed after greater than 90% confluency was reached on culture days 7-12. Cell cultures were maintained at 37°C in 5% CO₂ atmospheric conditions.

CDC assays with AQP4-transfected cells. CDC assays were performed using established protocols (21, 71). Cells were washed twice with F12 media (Gibco, Thermo Fisher Scientific) and incubated with serial dilutions of rAb or 5% patients' serum in F12 (for rAb) or MEM (for patients' serum) media containing 5% pooled human serum (Complement Technology) as a source of complement for 60 minutes at 37°C. LDH release was quantified using an LDH Cellular Cytotoxicity Kit (ClonTech). Absorbance at 490 nM was measured after 20 minutes of reaction development at room temperature using an absorbance plate reader (Molecular Devices). Complete LDH release (100%) was determined by lysing cells in a 1% Triton solution, and the background (no lysis) was determined by adding human serum to wells without AQP4 rAb. Cell death is presented as the percentage of lysis for all rAbs, calculated as (LDH experimental well - LDH background)/(LDH 100% lysis - LDH background) × 100%. Data were fitted to a sigmoidal 4-point binding curve to calculate CDC EC₅₀ values. For CDC assays using patients' serum, LDH release was normalized to heat-inactivated patients' serum alone, in the absence of supplemental human serum as a source of complement. Each treatment had 4

replicates per experiment. For experiments with peptide inhibitors, the final concentration of peptide was 40 μ M.

Primary astrocyte cultures for CDC assays. Astrocytes were washed and incubated with AQP4 rAb at 20 μ g/ml and 5% pooled human serum (Complement Technologies) as a source of human complement for 6 hours at 37°C. Dead cells were labeled with DRAQ7 (1:200; Abcam, 109202) and imaged with an IncuCyte Zoom system (Essen BioScience) as described previously (72). Briefly, each well was scanned with a $\times 10$ objective lens in 9 (for 24-well plates) or 4 (for 48-well plates) randomly selected positions with high-definition phase-contrast and epifluorescence microscopy using a 585-nm/635-nm filter. Image processing and cell counting were performed using IncuCyte software. Each treatment had 3 replicates per experiment. Experimental controls were 20 μ g/ml isotype control rAb plus 5% human serum.

AQP4 rAb-binding assays. Cells were washed twice in basal F12 media and incubated in live cell blocking buffer (MEM containing 2% NGS, 1% BSA, 1 mM NaPyr, 1 mM NEAA) for 30 minutes at 37°C. Serial dilutions of rAb were then applied in a live cell block for an additional 30 minutes at 37°C. Cells were washed once in basal MEM, fixed in chilled 4% PFA for 15 minutes, and washed 3 times in 1 \times PBS. Cells were blocked and permeabilized (10% NGS, 1% BSA, 1% Triton in 1 \times PBS) for 30 minutes, washed once in 1 \times PBS, and incubated for 30 minutes at room temperature in 5% NGS, 1% BSA, and 1 \times PBS with a commercial AQP4 antibody (1:200) recognizing an intracellular epitope (Santa Cruz Biotechnology, catalog sc-20812). Cells were washed 3 times in 1 \times PBS, and secondary antibodies (anti-human Alexa Fluor 594, A-11014, 1:400; anti-rabbit Alexa Fluor 488, A-11034, 1:400; Life Technologies, Thermo Fisher Scientific) were added for 30 minutes at room temperature in 2% NGS, 1% BSA, 1 \times PBS, followed by washes in 1 \times PBS. Binding affinity was calculated by nonlinear regression using a single-site, total-binding equation of background-subtracted red/green fluorescence intensity ratios. When CDC EC₅₀ values were superimposed over IgG-binding curves, the data points used to generate the curves were removed for clarity. Each experimental condition had 3 wells per treatment with at least 3 or more biologic replicates. AQP4 rAb ON 07-5 no. 53 or ON 07-5 no. 186 was tested in each experiment to confirm assay consistency. To quantify AQP4 expression without AQP4 rAb treatments, cells were fixed immediately after washing in basal F12 media, and immunohistochemistry was performed as above.

C1q-binding assays. Cells were washed twice in basal MEM media, and AQP4-specific or control rAb was added in the presence of 5% C4-depleted serum (Complement Technologies). After 30 minutes, cells were washed 3 times in basal MEM, and a FITC-conjugated anti-C1q antibody (Life Technologies, Thermo Fisher Scientific PA5-16601, 1:40) was added to live cell block solution for 30 minutes. Cells were washed once with basal MEM and fixed in chilled 4% PFA for 15 minutes. Three washes with 1 \times PBS were performed, and FITC fluorescence intensity was immediately quantified. Staining for AQP4 was then performed as described above. Data are represented as the fluorescence intensity ratio of C1q/AQP4 after background subtraction. When CDC EC₅₀ values were superimposed over C1q-binding curves, the data points used to generate the curves were removed for clarity. C1q binding to ON 07-5 no. 186 was tested in each experiment to confirm assay consistency.

C3d-binding assays. Cells were washed twice in basal F12 media, and AQP4-specific or control rAb was added in the presence of 5% C5-depleted serum (Complement Technologies). After 60 minutes,

cells were washed 3 times in basal F12, and a murine anti-C3d antibody (73) was added to live cell block solution for 30 minutes. Cells were washed twice with basal F12 and fixed in chilled 4% PFA for 15 minutes. AQP4 staining was performed as described above, with a C3d antibody secondary labeled with goat anti-mouse 594 (A-11032, 1:400, Life Technologies, Thermo Fisher Scientific). Images were acquired on a Leica DM IRB inverted microscope, and fluorescence was quantified using ImageJ software (NIH).

Models. Structural models were created using MacPyMOL version 1.7.4.4 (Schrodinger) and the crystal structures of AQP4 (Protein Data Bank [PDB] ID: 3GD8) (74), IgG1 (PDB ID: 1HZH) (75), IgG1 Fc domain (PDB ID: 1DN2) (33), C1q globular head (PDB ID: 1PK6) (76), and collagen (PDB ID: 2D3H) (77). C1q globular heads were joined to collagen assemblies on the basis of predicted structures (76, 78). For simplicity, the collagen stalk was removed from some C1q models.

STED super-resolution imaging and analysis. AQP4 rAb binding to cells was imaged using STED microscopy at a lateral resolution of less than 30 nm, with image acquisition, processing, and analysis performed as described previously (32). Briefly, bound AQP4 rAbs were labeled with Atto647N (Atto Tec), and AQP4 tetramers are detected with anti-rabbit STAR590 (Rockland). STED microscopy was performed (minimum 3 images per AQP4 rAb) using a noncommercial STED microscope at the University of Colorado's Anschutz Light Microscopy Core. A series of MATLAB (R2015a software) programs were coded in-house to quantify the average size of all membrane-bound AQP4 rAb clusters across the entire STED image. Cluster spreading was calculated as the full width at half maximum (FWHM) of a resolvable object. The potential for multivalent C1q contacts (termed the ASA score) was quantified as previously described (32). Here, the rAb cluster spread was grouped by rAb epitope specificity and the ASA score distributions analyzed using unbiased hierarchical clustering analysis in the Statistics and Machine Learning Toolbox in MATLAB. To correlate epitope-dependent antibody clustering with metrics of rAb binding, C1q binding, and CDC, ASA score distributions were converted into a mean score of 1 to 4 using the following formula: mean ASA = 1 \times (% distribution ASA score 1) + 2 \times (% distribution ASA score 2) + 3 \times (% distribution ASA score 3) + 4 \times (% distribution ASA score 4).

STORM imaging and analysis. Primary cerebellar and cortical murine astrocyte cultures were grown on glass-bottomed Petri dishes (MatTek). Intracellular AQP4 immunostaining was performed (32) and detected with anti-rabbit Alexa Fluor 647 (A-21244, 1:200, Life Technologies, Thermo Fisher Scientific). STORM imaging of AQP4 membrane protein was performed on a commercial Zeiss Elyra P.1 Imaging System at the Anschutz Medical Campus Light Microscopy Core, using STORM imaging buffer (50 mM Tris-HCl, 10 mM NaCl, 10% glucose with ethanolamine, glucose oxidase, and catalase). At least 20,000 frames were acquired per image, and image processing was performed using the Zeiss software package including drift correction, filtering of continuous blinking signal, and resolution quantification. AQP4 expression was then estimated using an adapted binary threshold algorithm (33) for identically sized regions of interest randomly chosen within each imaged cell.

Alexa Fluor 647 fluorophore resolution was characterized using M1-AQP4-transfected CHO cells. AQP4 rAbs genetically tagged with mGeos (79) were first bound to M1-AQP4 CHO cells using the live cell rAb-binding protocol and then intracellularly stained as described above to label individual AQP4 tetramers with Alexa Fluor 647. rAb

signal was processed and used to mask the Alexa Fluor 647 channel, and resolution was calculated for all underlying AQP4 tetramers. Resolution was consistent when imaging randomly immobilized secondary antibodies on glass dishes, with TetraSpeck fiducial markers (Thermo Fisher Scientific) randomly immobilized to establish the plane of focus.

Statistics. Statistical analyses were performed using GraphPad Prism 6 (GraphPad Software). For all analyses, a *P* value of less than 0.05 was considered statistically significant.

Study approval. Written informed consent was received from all participants prior to inclusion in the study. This study was approved by the IRB at the University of Colorado Anschutz Medical Campus.

Author contributions

JS and YL performed experiments. AR, SW, and KS cloned AQP4 rAb. HS produced AQP4 rAbs. JS, YL, GPO, and JLB analyzed

data, prepared the figures, and edited the manuscript. JLB conceived the project.

Acknowledgments

We thank the Anschutz Medical Campus Light Microscopy Core for providing access to the STED microscope and assistance with STED imaging. This work was funded by the NIH (R01EY022936 and UM1 AI110498, to JLB); a National Multiple Sclerosis Society Collaborative Grant; and the Guthy-Jackson Charitable Foundation. JS is a trainee of and has received support from the Medical Scientist Training Program at the University of Colorado Anschutz Medical Campus (MSTP T32 GM008497).

Address correspondence to: Jeffrey L. Bennett, 12700 E. 19th Avenue, Box B-182, Aurora, Colorado 80045, USA. Phone: 303.724.4312; Email: jeffrey.bennett@ucdenver.edu.

- Wingerchuk DM, et al. International consensus diagnostic criteria for neuromyelitis optica spectrum disorders. *Neurology*. 2015;85(2):177-189.
- Lennon VA, Kryzer TJ, Pittock SJ, Verkman AS, Hinson SR. IgG marker of optic-spinal multiple sclerosis binds to the aquaporin-4 water channel. *J Exp Med*. 2005;202(4):473-477.
- Jarius S, Wildemann B. AQP4 antibodies in neuromyelitis optica: diagnostic and pathogenetic relevance. *Nat Rev Neurol*. 2010;6(7):383-392.
- Waters PJ, et al. Serologic diagnosis of NMO: a multicenter comparison of aquaporin-4-IgG assays. *Neurology*. 2012;78(9):665-671.
- Ratelade J, Verkman AS. Neuromyelitis optica: aquaporin-4 based pathogenesis mechanisms and new therapies. *Int J Biochem Cell Biol*. 2012;44(9):1519-1530.
- Papadopoulos MC, Bennett JL, Verkman AS. Treatment of neuromyelitis optica: state-of-the-art and emerging therapies. *Nat Rev Neurol*. 2014;10(9):493-506.
- Misu T, et al. Presence of six different lesion types suggests diverse mechanisms of tissue injury in neuromyelitis optica. *Acta Neuropathol*. 2013;125(6):815-827.
- Lachmann PJ, Hughes-Jones NC. Initiation of complement activation. *Springer Semin Immunopathol*. 1984;7(2-3):143-162.
- Ricklin D, Hajishengallis G, Yang K, Lambris JD. Complement: a key system for immune surveillance and homeostasis. *Nat Immunol*. 2010;11(9):785-797.
- Bennett JL, et al. Intrathecal pathogenic anti-aquaporin-4 antibodies in early neuromyelitis optica. *Ann Neurol*. 2009;66(5):617-629.
- Phuan PW, et al. C1q-targeted monoclonal antibody prevents complement-dependent cytotoxicity and neuropathology in in vitro and mouse models of neuromyelitis optica. *Acta Neuropathol*. 2013;125(6):829-840.
- Phuan PW, Ratelade J, Rossi A, Tradtrantip L, Verkman AS. Complement-dependent cytotoxicity in neuromyelitis optica requires aquaporin-4 protein assembly in orthogonal arrays. *J Biol Chem*. 2012;287(17):13829-13839.
- Asavapanumas N, Verkman AS. Neuromyelitis optica pathology in rats following intraperitoneal injection of NMO-IgG and intracerebral needle injury. *Acta Neuropathol Commun*. 2014;2:48.
- Asavapanumas N, Ratelade J, Verkman AS. Unique neuromyelitis optica pathology produced in naïve rats by intracerebral administration of NMO-IgG. *Acta Neuropathol*. 2014;127(4):539-551.
- Verkman AS, Ratelade J, Rossi A, Zhang H, Tradtrantip L. Aquaporin-4: orthogonal array assembly, CNS functions, and role in neuromyelitis optica. *Acta Pharmacol Sin*. 2011;32(6):702-710.
- Hinson SR, et al. Pathogenic potential of IgG binding to water channel extracellular domain in neuromyelitis optica. *Neurology*. 2007;69(24):2221-2231.
- Hinson SR, et al. Molecular outcomes of neuromyelitis optica (NMO)-IgG binding to aquaporin-4 in astrocytes. *Proc Natl Acad Sci U S A*. 2012;109(4):1245-1250.
- Hinson SR, McKeon A, Fryer JP, Apiwattanakul M, Lennon VA, Pittock SJ. Prediction of neuromyelitis optica attack severity by quantitation of complement-mediated injury to aquaporin-4-expressing cells. *Arch Neurol*. 2009;66(9):1164-1167.
- Owens GP, et al. Mutagenesis of the aquaporin 4 extracellular domains defines restricted binding patterns of pathogenic neuromyelitis optica IgG. *J Biol Chem*. 2015;290(19):12123-12134.
- Iorio R, et al. Astrocytic autoantibody of neuromyelitis optica (NMO-IgG) binds to aquaporin-4 extracellular loops, monomers, tetramers and high order arrays. *J Autoimmun*. 2013;40:21-27.
- Tradtrantip L, et al. Anti-aquaporin-4 monoclonal antibody blocker therapy for neuromyelitis optica. *Ann Neurol*. 2012;71(3):314-322.
- Crane JM, Lam C, Rossi A, Gupta T, Bennett JL, Verkman AS. Binding affinity and specificity of neuromyelitis optica autoantibodies to aquaporin-4 M1/M23 isoforms and orthogonal arrays. *J Biol Chem*. 2011;286(18):16516-16524.
- Gaboriaud C, Ling WL, Thielens NM, Bally I, Rossi V. Deciphering the fine details of c1 assembly and activation mechanisms: "mission impossible"? *Front Immunol*. 2014;5:565.
- Merle NS, Church SE, Fremiaux-Bacchi V, Roumenina LT. Complement system part I - molecular mechanisms of activation and regulation. *Front Immunol*. 2015;6:262.
- Diebolder CA, et al. Complement is activated by IgG hexamers assembled at the cell surface. *Science*. 2014;343(6176):1260-1263.
- de Jong RN, et al. A novel platform for the potentiation of therapeutic antibodies based on antigen-dependent formation of IgG hexamers at the cell surface. *PLoS Biol*. 2016;14(1):e1002344.
- Cook EM, et al. Antibodies That efficiently form hexamers upon antigen binding can induce complement-dependent cytotoxicity under complement-limiting conditions. *J Immunol*. 2016;197(5):1762-1775.
- Tradtrantip L, Felix CM, Spirig R, Morelli AB, Verkman AS. Recombinant IgG1 Fc hexamers block cytotoxicity and pathological changes in experimental in vitro and rat models of neuromyelitis optica. *Neuropharmacology*. 2018;133:345-353.
- Moore GL, Chen H, Karki S, Lazar GA. Engineered Fc variant antibodies with enhanced ability to recruit complement and mediate effector functions. *MAbs*. 2010;2(2):181-189.
- Crane JM, Verkman AS. Determinants of aquaporin-4 assembly in orthogonal arrays revealed by live-cell single-molecule fluorescence imaging. *J Cell Sci*. 2009;122(6):813-821.
- Furman CS, et al. Aquaporin-4 square array assembly: opposing actions of M1 and M23 isoforms. *Proc Natl Acad Sci U S A*. 2003;100(23):13609-13614.
- Soltys JN, Meyer SA, Schumann H, Gibson EA, Restrepo D, Bennett JL. Determining the spatial relationship of membrane-bound aquaporin-4 autoantibodies by STED nanoscopy. *Biophys J*. 2017;112(8):1692-1702.
- Smith AJ, Verkman AS. Superresolution imaging of aquaporin-4 cluster size in antibody-stained paraffin brain sections. *Biophys J*. 2015;109(12):2511-2522.
- Hubbard JA, Hsu MS, Seldin MM, Binder DK. Expression of the astrocyte water channel aquaporin-4 in the mouse brain. *ASN Neuro*. 2015;7(5):1759091415605486.
- DeLano WL, Ultsch MH, de Vos AM, Wells JA. Convergent solutions to binding at a protein-protein interface. *Science*. 2000;287(5456):1279-1283.
- Rossi A, Moritz TJ, Ratelade J, Verkman AS. Super-resolution imaging of aquaporin-4 orthog-

- onal arrays of particles in cell membranes. *J Cell Sci.* 2012;125(Pt 18):4405–4412.
37. Ratelade J, Bennett JL, Verkman AS. Evidence against cellular internalization in vivo of NMO-IgG, aquaporin-4, and excitatory amino acid transporter 2 in neuromyelitis optica. *J Biol Chem.* 2011;286(52):45156–45164.
 38. Gaboriaud C, Thielens NM, Gregory LA, Rossi V, Fontecilla-Camps JC, Arlaud GJ. Structure and activation of the C1 complex of complement: unraveling the puzzle. *Trends Immunol.* 2004;25(7):368–373.
 39. Wallis R, Mitchell DA, Schmid R, Schwaebler WJ, Keeble AH. Paths reunited: Initiation of the classical and lectin pathways of complement activation. *Immunobiology.* 2010;215(1):1–11.
 40. Wang G, et al. Molecular basis of assembly and activation of complement component C1 in complex with immunoglobulin G1 and antigen. *Mol Cell.* 2016;63(1):135–145.
 41. Pittock SJ, Weinschenker BG, Lucchinetti CF, Wingerchuk DM, Corboy JR, Lennon VA. Neuromyelitis optica brain lesions localized at sites of high aquaporin 4 expression. *Arch Neurol.* 2006;63(7):964–968.
 42. Matiello M, Schaefer-Klein J, Sun D, Weinschenker BG. Aquaporin 4 expression and tissue susceptibility to neuromyelitis optica. *JAMA Neurol.* 2013;70(9):1118–1125.
 43. Verkman AS. Aquaporins in clinical medicine. *Annu Rev Med.* 2012;63:303–316.
 44. Ratelade J, Bennett JL, Verkman AS. Intravenous neuromyelitis optica autoantibody in mice targets aquaporin-4 in peripheral organs and area postrema. *PLoS One.* 2011;6(11):e27412.
 45. McCullough JW, Renner B, Thurman JM. The role of the complement system in acute kidney injury. *Semin Nephrol.* 2013;33(6):543–556.
 46. Holers VM. Complement and its receptors: new insights into human disease. *Annu Rev Immunol.* 2014;32:433–459.
 47. Zhang H, Verkman AS. Longitudinally extensive NMO spinal cord pathology produced by passive transfer of NMO-IgG in mice lacking complement inhibitor CD59. *J Autoimmun.* 2014;53:67–77.
 48. Yao X, Verkman AS. Complement regulator CD59 prevents peripheral organ injury in rats made seropositive for neuromyelitis optica immunoglobulin G. *Acta Neuropathol Commun.* 2017;5(1):57.
 49. Verkman AS, Yao X, Smith AJ. The evolving mystery of why skeletal muscle is spared in seropositive neuromyelitis optica. *J Cell Mol Med.* 2018;22(3):2039–2040.
 50. Crane JM, Bennett JL, Verkman AS. Live cell analysis of aquaporin-4 m1/m23 interactions and regulated orthogonal array assembly in glial cells. *J Biol Chem.* 2009;284(51):35850–35860.
 51. Martinez-Hernandez E, Horvath J, Shiloh-Malawsky Y, Sangha N, Martinez-Lage M, Dalmau J. Analysis of complement and plasma cells in the brain of patients with anti-NMDAR encephalitis. *Neurology.* 2011;77(6):589–593.
 52. Hughes EG, et al. Cellular and synaptic mechanisms of anti-NMDA receptor encephalitis. *J Neurosci.* 2010;30(17):5866–5875.
 53. Engel AG, Fumagalli G. Mechanisms of acetylcholine receptor loss from the neuromuscular junction. *Ciba Found Symp.* 1982;(90):197–224.
 54. Drachman DB, Angus CW, Adams RN, Michelson JD, Hoffman GJ. Myasthenic antibodies cross-link acetylcholine receptors to accelerate degradation. *N Engl J Med.* 1978;298(20):1116–1122.
 55. Tüzün E, Christodoss P. Complement associated pathogenic mechanisms in myasthenia gravis. *Autoimmun Rev.* 2013;12(9):904–911.
 56. Howard JF, et al. Safety and efficacy of eculizumab in anti-acetylcholine receptor antibody-positive refractory generalised myasthenia gravis (REGAIN): a phase 3, randomised, double-blind, placebo-controlled, multicentre study. *Lancet Neurol.* 2017;16(12):976–986.
 57. Shimizu F, et al. Glucose-regulated protein 78 autoantibody associates with blood-brain barrier disruption in neuromyelitis optica. *Sci Transl Med.* 2017;9(397):eaai9111.
 58. Tradtrantip L, Asavapanumas N, Verkman AS. Therapeutic cleavage of anti-aquaporin-4 autoantibody in neuromyelitis optica by an IgG-selective proteinase. *Mol Pharmacol.* 2013;83(6):1268–1275.
 59. Tradtrantip L, Ratelade J, Zhang H, Verkman AS. Enzymatic deglycosylation converts pathogenic neuromyelitis optica anti-aquaporin-4 immunoglobulin G into therapeutic antibody. *Ann Neurol.* 2013;73(1):77–85.
 60. Quast I, et al. Sialylation of IgG Fc domain impairs complement-dependent cytotoxicity. *J Clin Invest.* 2015;125(11):4160–4170.
 61. Lewis LA, Ram S. Meningococcal disease and the complement system. *Virulence.* 2014;5(1):98–126.
 62. Trouw LA, et al. Anti-C1q autoantibodies deposit in glomeruli but are only pathogenic in combination with glomerular C1q-containing immune complexes. *J Clin Invest.* 2004;114(5):679–688.
 63. Burgoon MP, et al. Cloning the antibody response in humans with inflammatory CNS disease: isolation of measles virus-specific antibodies from phage display libraries of a subacute sclerosing panencephalitis brain. *J Neuroimmunol.* 1999;94(1–2):204–211.
 64. Owens GP, et al. VH4 gene segments dominate the intrathecal humoral immune response in multiple sclerosis. *J Immunol.* 2007;179(9):6343–6351.
 65. Kabat K, Wu TT, Perry HM, Gottesman KS, Foeller C. *Sequences of Proteins of Immunological Interest*, 5th ed. Bethesda, Maryland, USA: United States Public Health Service, National Institutes of Health; 1991.
 66. Owens GP, et al. Screening random peptide libraries with subacute sclerosing panencephalitis brain-derived recombinant antibodies identifies multiple epitopes in the C-terminal region of the measles virus nucleocapsid protein. *J Virol.* 2006;80(24):12121–12130.
 67. Liu Y, Vidensky S, Ruggiero AM, Maier S, Sitte HH, Rothstein JD. Reticulon RTN2B regulates trafficking and function of neuronal glutamate transporter EAAC1. *J Biol Chem.* 2008;283(10):6561–6571.
 68. Feldmann M, Pathipati P, Sheldon RA, Jiang X, Ferriero DM. Isolating astrocytes and neurons sequentially from postnatal murine brains with a magnetic cell separation technique. *J Biol Methods.* 2014;1(2):e11.
 69. Jungblut M, et al. Isolation and characterization of living primary astroglial cells using the new GLAST-specific monoclonal antibody ACSA-1. *Glia.* 2012;60(6):894–907.
 70. Batiuk MY, et al. An immunofluorescence-based method for isolating ultrapure adult astrocytes based on ATP1B2 targeting by the ACSA-2 antibody. *J Biol Chem.* 2017;292(21):8874–8891.
 71. Mader S, Brimberg L, Soltys JN, Bennett JL, Diamond B. Mutations of recombinant aquaporin-4 antibody in the Fc domain can impair complement-dependent cellular cytotoxicity and transplacental transport. *Front Immunol.* 2018;9:1599.
 72. Liu Y, Harlow DE, Given KS, Owens GP, Macklin WB, Bennett JL. Variable sensitivity to complement-dependent cytotoxicity in murine models of neuromyelitis optica. *J Neuroinflammation.* 2016;13(1):301.
 73. Thurman JM, et al. Detection of complement activation using monoclonal antibodies against C3d. *J Clin Invest.* 2013;123(5):2218–2230.
 74. Ho JD, et al. Crystal structure of human aquaporin 4 at 1.8 Å and its mechanism of conduction. *Proc Natl Acad Sci U S A.* 2009;106(18):7437–7442.
 75. Sapphire EO, et al. Crystal structure of a neutralizing human IGG against HIV-1: a template for vaccine design. *Science.* 2001;293(5532):1155–1159.
 76. Gaboriaud C, et al. The crystal structure of the globular head of complement protein C1q provides a basis for its versatile recognition properties. *J Biol Chem.* 2003;278(47):46974–46982.
 77. Okuyama K, et al. High-resolution structures of collagen-like peptides [(Pro-Pro-Gly)4-Xaa-Yaa-Gly-(Pro-Pro-Gly)4]: implications for triple-helix hydration and Hyp(X) puckering. *Biopolymers.* 2009;91(5):361–372.
 78. Rainey JK, Goh MC. A statistically derived parameterization for the collagen triple-helix. *Protein Sci.* 2002;11(11):2748–2754.
 79. Chang H, et al. A unique series of reversibly switchable fluorescent proteins with beneficial properties for various applications. *Proc Natl Acad Sci U S A.* 2012;109(12):4455–4460.